




Studies of microstructural, dielectric, and impedance spectroscopic properties of $\text{Bi}_{0.617}\text{Y}_{0.05}\text{Cu}_3\text{Ti}_4\text{O}_{12}$ ceramic synthesized through semi-wet route

Dinesh Prajapati¹, Vishnu Shankar Rai¹, Santosh Pandey¹, Vinod Kumar¹, Manish Kumar Verma¹, Atendra Kumar¹, Shruti Singh¹, Kedar Sahoo², and K. D. Mandal^{1,*} 

¹Department of Chemistry, Indian Institute of Technology Banaras Hindu University, Varanasi, UP 221005, India

²Department of Chemical Engineering, Indian Institute of Technology Banaras Hindu University, Varanasi, UP 221005, India

Received: 7 April 2021

Accepted: 9 September 2021

Published online:
28 September 2021

© The Author(s), under exclusive licence to Springer Science+Business Media, LLC, part of Springer Nature 2021

ABSTRACT

$\text{Bi}_{0.617}\text{Y}_{0.05}\text{Cu}_3\text{Ti}_4\text{O}_{12}$ (BYCTO) was successfully synthesized through an economically semi-wet route using metals nitrates, acetate, and TiO_2 precursor and sintered at 1173 K for 8 h. The single phase of ceramic was authorized by XRD analysis. The crystallite size of BYCTO ceramic was calculated to be 62.3 nm through XRD measurement. The particle size obtained by TEM analysis was to be in the range of 55 ± 7 nm. The average grain size observed through the SEM technique was 0.783 μm . The route means square roughness, as well as average roughness, were determined to be 0.224 μm and 0.179 μm by atomic force microscope. The dielectric constant (ϵ') of BYCTO was measured to be 1481 at 307 K and 100 Hz. The tangent loss ($\tan \delta$) was observed to be in the range of 0.13–0.29 at all selected temperatures (307–487 K) and 10 kHz which is lower than that of $\text{Bi}_{2/3}\text{Cu}_3\text{Ti}_4\text{O}_{12}$. The oxidation state of all metal present in the ceramic material was verified by XPS analysis.

1 Introduction

Since Subramaniam discovered the enormously high dielectric response perovskite material $\text{CaCu}_3\text{Ti}_4\text{O}_{12}$ (CCTO) in 2000 [1]. It displays an exceedingly colossal dielectric constant of around 10^4 – 10^5 at room temperature, which is roughly 10^2 – 10^6 Hz independent in frequency ranges. Compared with other materials that have a giant dielectric constant, such as BaTiO_3 -based ceramics without ferroelectric phase transition, CCTO has excellent temperature stability

over a large range of 100–600 K [2]. Due to giant dielectric permittivity, CCTO materials have been used for numerous technological applications in electronic devices such as capacitors, switching, gas sensing devices, energy storage devices, and microwave communication devices [3–5]. The body-centered cubic structure has been found in CCTO based ceramics of which it has a lattice parameter of 7.391 Å and space group Im3 [6, 7]. Ferroelectric substances typically display a high dielectric constant value and this is related to atomic displacement with

Address correspondence to E-mail: kdmandal.apc@itbhu.ac.in

a non-Centro symmetrical shape [8]. The dielectric, as well as magnetic behaviour, have been enhanced by doping of numerous cationic substituents at Cu and Ti-site in $\text{CaCu}_3\text{Ti}_4\text{O}_{12}$ (CCTO) [9]. Researchers have published several models of intrinsic and extrinsic mechanisms over the past decade to discover the origin of the CCTO's giant dielectric constant [10–12]. Instead of an intrinsic property related to the crystal structure and the extrinsic mechanism related to grain boundaries properties have been explained based on the internal layer capacitor (IBLC) model to improving the dielectric behaviour of CCTO ceramics. This model has also described that CCTO ceramics consist of n-type semiconducting grains and insulating grain boundaries. Due to the IBLC phenomenon, electric charge in huge amounts will gather at the interface of grain and grain boundaries because of the impact of the electric field therefore this behaviour of charge would greatly increase the dielectric response [2]. CCTO ceramic studies by impedance spectroscopy show that semiconducting grains and insulating grain boundaries are heterogeneous [13, 14]. Bismuth copper titanate (BCTO) ($\text{Bi}_{2/3}\text{Cu}_3\text{Ti}_4\text{O}_{12}$) has rarely been investigated as a member of the titanate family with a general formula of $\text{ACu}_3\text{Ti}_4\text{O}_{12}$ (where $A_{1/4}$ Ba, Ca, Sr, $\text{Gd}_{2/3}$, $\text{Pr}_{2/3}$, $\text{Y}_{2/3}$, $\text{Bi}_{2/3}$ or $\text{La}_{2/3}$). However, some researchers have attempted to synthesize BCTO [15–17]. L. Yang et al. was synthesized BCTO with the help of a solid-state reaction method that has achieved a huge dielectric constant of approximately 3.3×10^5 at 1 kHz [18]. The big task is that to obtain high dielectric constant and acceptable low dielectric loss materials continue as an issue. Lots of work have been done on metals doping. Sun et al. reported that $\text{CaCu}_3\text{Ti}_{3.95}\text{Zr}_{0.05}\text{O}_{12}$ ceramics have dielectric loss below 0.05 in a wide frequency range [19]. Saji et al. found that at $x = 0.02$, $\text{CaCu}_3\text{Ti}_{4-x}\text{Y}_x\text{O}_{12-x/2}$ films showed a low $\tan \delta \sim 0.07$ at 1 kHz [20]. Luo et al. found that at $x = 0.05$, $\text{CaCu}_3\text{Ti}_{4-x}\text{Y}_x\text{O}_{12-x/2}$ ceramics decrease the loss below 0.1 at the frequency range from 1 to 300 kHz, but maintain a high dielectric constant [21]. Sharma et al. reported recently that $\text{Y}_{2/3}\text{Cu}_3\text{Ti}_4\text{O}_{12}$ (YCTO) ceramic has very high dielectric constant (8434) and also high dielectric constant (3.5) at room temperature and 100 Hz frequency [22]. In literature, the BCTO ($\text{Bi}_{2/3}\text{Cu}_3\text{Ti}_4\text{O}_{12}$) is isostructural with CCTO and YCTO. It indicates the temperature and frequency dependence of dielectric as CCTO [18, 23]. We have also observed in the literature that BCTO

ceramic has a very high dielectric constant of nearly 2.9×10^4 at 323 K and a high dielectric loss of approximately 3.0 at 100 Hz, which was prepared by the semi-wet route. Due to which it has been used in potential applications and also its magnetic studies show paramagnetic to the superparamagnetic phase transition [24].

To this extent, we have reported studies of synthesis, microstructures, and effect on dielectric and impedance properties of BCTO ceramic by partial substitution of Yttrium (Y) on Bi site because Bi and Y have trivalent and the crystal radii of Bi (1.10 Å) and Y (1.02 Å) are comparable to each other. The dielectric properties of the Y-doped ceramic synthesised through a semi-wet route, as well as its microstructural properties, were examined and described. Furthermore, the optical energy gap study of semiconducting BYCTO ceramic is an important aspect for establishing the dielectric nature. Therefore, the Kubelka–Munk theory based on the diffuse reflectance study provides important insight into the band structure of prepared ceramic. It is described as

$$F(R) = \frac{\alpha}{S} = \frac{(1 - R)^2}{2R} \quad (1)$$

$F(R)$: Kubelka–Munk function, α : absorption coefficient, R : reflectance, S : scattering factor.

The resulting optical bandgap can be determined by plotting diffuse reflectance versus wavelength, where the onset of a linear increase in the curve defines the corresponding bandgap energy. However, since this method of measuring bandgap energy produces slightly inaccurate results, the form of transition (direct/indirect) must be recorded during evaluation. absorption edge analysis was used to evaluate the form of transition. The optical bandgap represented in Eq. 2

$$\alpha h\nu = k * (h\nu - E_g)^{1/n} \quad (2)$$

where k^* , E_g are the energy-independent constant and optical bandgap. The exponent n defines the type of transition where the value of $n = 2$ and $1/2$ for direct and indirect allowed transitions, respectively. Since $F(R)$ is proportional to α , a modified form of Eq. 2 can be represented as

$$F(R) * h\nu = k * (h\nu - E_g)^{1/n} \quad (3)$$

The giant dielectric constant ceramics, all have micro-sized grains, and the dielectric constant has

been discovered to increase as grain size increases, preventing the downsizing of smaller and quicker electronic components. Various methods have been used earlier to synthesize the CCTO ceramics mostly state reaction technique through multi-step calcinations processes at high temperatures, leading to microcrystalline powder, mechanical milling, sol-gel, polymerization, and other wet chemical methods are also used to prepare nanocrystalline CCTO powder. However, traditional sintering of micro- and nano-crystalline CCTO powder (generally at high temperatures > 1000 °C for long periods at a time between 3 and 48 h) results in coarse-grained CCTO ceramics with grain sizes ranging from a few to 300 μm . When CCTO nano ceramics were prepared by mechanochemical synthesis and spark plasma sintering at 1050 °C for 10 h to study the effect of grain size on high dielectric constant [25]. It was found that grain size considerably about 2–3 μm but conventional sintering of the same mechano-synthesized CCTO nano-powder at 1050 °C for 10 h leads to CCTO ceramics with the grain size of 20 μm [26]. The average grain size of the BCTO ceramic prepared semi-wet route at 1073 K for 8 h was found to be in the range of 0.73 ± 0.2 μm [24]. So our purpose is to reduce the grain size synthesized by semi-wet route.

2 Material synthesis

The $\text{Bi}_{0.617}\text{Y}_{0.05}\text{Cu}_3\text{Ti}_4\text{O}_{12}$ referred to as the BYCTO sample was prepared by a semi-wet route. In this synthesis, we have used chemicals such as Bismuth nitrate $\text{Bi}(\text{NO}_3)_3 \cdot 5\text{H}_2\text{O}$ (99% Merck, India), $\text{Y}(\text{NO}_3)_3 \cdot 6\text{H}_2\text{O}$ [99.8% obtained from HiMedia, Mumbai, India], copper acetate $\text{Cu}(\text{CH}_3\text{COO})_2 \cdot \text{H}_2\text{O}$ (99% Merck, India) and titanium oxide TiO_2 (98.5% Merck, India), were used in stoichiometric ratio as starting materials. We prepared the solution of Bismuth nitrate $\text{Bi}(\text{NO}_3)_3 \cdot 5\text{H}_2\text{O}$ (99% Merck, India), copper acetate $\text{Cu}(\text{CH}_3\text{COO})_2 \cdot \text{H}_2\text{O}$ (99% Merck, India) separately in beakers with double-distilled water and blended all solutions in the beaker. Solid TiO_2 was added in solution with a stoichiometric amount. The whole solution was heated by putting it on a hot plate magnetic stirrer and maintained the temperature of the stirrer about 348–353 K for 12–15 h. The calculated amount of Citric acid generally equivalent to metal ions was mixed with distilled water and added slowly in solution because citric

acid act as organic fuel for the solution as well as used as a complexing agent in the ignition step, due to these properties it helps in mixing very well. After continuous heating the solution, i.e., evaporation of water, a slurry form was obtained that allows self-ignitions [27]. We were obtained a fluffy mass of BYCTO samples after removing a lot of gases. The resulting BYCTO material was changed into fine powders with the help of agate and mortar. The powder was calcined at 1073 K for 6 h and mixed with 2% PVA solution as a binder and dry it in furnace at 673 K for 2 h to remove PVA. After this, obtained powder undergoes palletization with the help of hydraulic press by applying pressure 4–5 ton using hydraulic pressure for 2 min. At last, the pallets were sintered at 1173 K for 8 h.

3 Material characterization

The elemental compositions and microstructure of sintered sample were observed by an energy-dispersive X-ray (EDX) analyser (Oxford instrument, USA) attached with the scanning electron microscope. The particle size was confirmed by a high-resolution transmission electron microscope (HR-TEM, Technai G2 20 S-Twin). To make a sample for HR-TEM characterization. The sintered sample was disseminated in acetone and sonicated for 90 min. This suspension was applied on a carbon-coated copper grid and dried in an oven for 5 h. The surface morphology and thickness were examined with the help of atomic force microscopy (NTEGRA Prima, Germany). The crystalline phase of $\text{Bi}_{0.617}\text{Y}_{0.05}\text{Cu}_3\text{Ti}_4\text{O}_{12}$ (BYCTO) ceramic-sintered samples was recognized by an X-ray diffractometer (Rigaku miniflex 600, Japan) employing $\text{Cu-K}\alpha$ radiation with wavelength 1.5418 Å. For dielectric and electrical measurements of pallets which were polished and coated by silver paste on both sides and then kept at 150 °C for 50 min to form electrodes for electrical characterization. The capacitance (C), tangent loss or dielectric loss ($\tan \delta$) and conductance (G) were measured from LCR meter (PSM1735-NumetriQ, Newton 4th Ltd, UK) with variation of temperature and frequencies. From these data, the dielectric constant and conductivity of the sample were determined using the sample dimension. The oxidation state was confirmed by X-ray photoelectron spectroscopy (XPS) using Thermo Fisher Scientific $\text{K}\alpha$

(Waltham, MA) in broad scan survey mode and high energy resolution with $\text{AlK}\alpha$ (1486.6 eV). Balance deuterium halogen source (DH 2000 BAL, Ocean Optics) is used for recording the reflection spectra under the spectral range 210–2500 nm. Optical bandgap energy of BYCTO ceramic was extracted from the detected diffuse reflectance spectra.

4 Results and discussion

4.1 X-ray diffraction (XRD) analysis

Figure 1a shows the XRD pattern of $\text{Bi}_{0.617}\text{Y}_{0.05}\text{Cu}_3\text{Ti}_4\text{O}_{12}$ ceramics material referred to as BYCTO of single dopant sintered at 1173 K for 8 h which indeed exhibits the single-phase formation of BYCTO ceramic with a body-centered cubic structure takes place. The main XRD diffraction peaks of BYCTO ceramic corresponding to (200), (211), (220), (310), (222), (321), (400), (422), (440) planes were acceptably matched with BCTO (JCPDS card No. 46-0725) [28]. XRD pattern was indexed based on a body-centered cubic structure of BCTO ceramic.

Rietveld refinement of the XRD pattern for $\text{Bi}_{0.617}\text{Y}_{0.05}\text{Cu}_3\text{Ti}_4\text{O}_{12}$ ceramic were carried out with the help of Fullproff software is shown in Fig. 1b. It is inferred from the figure that both of the calculated pattern assigned by red circle and experimentally observed pattern assigned by the black circles are exactly overlapped to each other's which indicates the good fitting of the XRD data. The lower value of χ^2 ,

Bragges reflections and difference between calculated pattern and experimental observed pattern and their peak positions also confirmed single phase formation of $\text{Bi}_{0.617}\text{Y}_{0.05}\text{Cu}_3\text{Ti}_4\text{O}_{12}$ ceramic along with body-centered cubic structure and space group Im-3 [29]. The refined cell parameters, Phase with the Space group, Bragg R-factor, RF factor, refined half-width parameters, and Reliability factor of BYCTO ceramic are mentioned in Table 1. The goodness of fit R_p/R_{wp} and χ^2 observed from the retviold refinement was found to be 1.39 and 2.84 respectively inferred the reasonable refinement of the XRD result. The refined value of atomic position and occupancy for BYCTO ceramic observed during the refinement is mentioned in Table. 2.

The crystallite size BYCTO ceramic material was calculated by the Debye–Scherrer formula which has been given below:

$$D = \frac{k\lambda}{\beta \cos \theta} \quad (4)$$

where D , λ , θ and β are the crystallite size, the wavelength of X-ray (0.15418 Å), Bragg diffraction angle, and full width at half maximum (FWHM) in radians. k is crystal shape coefficient (0.89). The line broadening occurred due to instrumental effect has been removed with the help of a standard sample (silicon wafer) for XRD data to determine the exact value of crystallite size. The average crystallite size of the BYCTO sample at Y-doping concentration was calculated to be 62.3 nm.

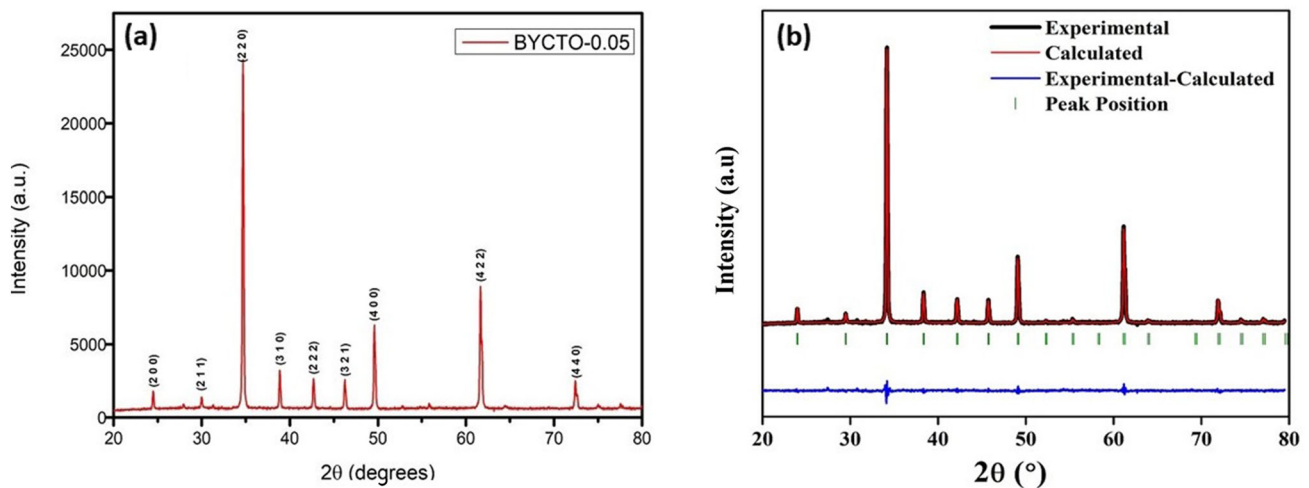


Fig. 1 a XRD pattern of $\text{Bi}_{0.617}\text{Y}_{0.05}\text{Cu}_3\text{Ti}_4\text{O}_{12}$ ceramic sintered at 1173 K for 8 h; b shows the Le Bail full pattern matching analysis of XRD patterns for $\text{Bi}_{0.617}\text{Y}_{0.05}\text{Cu}_3\text{Ti}_4\text{O}_{12}$ ceramic

Table 1 The refined cell parameters, Phase with the Space group, Bragg R-factor, RF factor, refined half-width parameters, and reliability factor of BYCTO ceramic

	χ^2 : 2.84		
Refined cell parameters (Å)	$a = b = c = 7.42091$	Angle	$\alpha = \beta = \gamma = 90^\circ$
Phase	BCC	Space group of phase	$I m \bar{3}$
Bragg R-factor (%)	3.63	RF factor (%)	4.46
Refined half-width parameters	$U = 0$	$V = -0.004473$	$W = 0.009538$
Reliability factor (%)	$R_p = 19.2$	$R_{wp} = 13.8$	$R_{exp} = 8.16$

Table 2 The refined Chi-square (χ^2) value, refined coordinates and occupancy of BYCTO ceramic

χ^2 : 2.84					
Atom	Ion	x	y	z	Occupancy
Bi	Bi^{3+}	0.00000	0.00000	0.00000	0.01699
Cu	Cu^{2+}	0.00000	0.50000	0.50000	0.09952
Ti	Ti^{4+}	0.00000	0.00000	0.00000	0.15119
O	O^{2-}	0.18070	0.30194	0.00000	0.47078

4.2 Microstructural studies

4.2.1 Transmission electron microscopic (TEM) studies

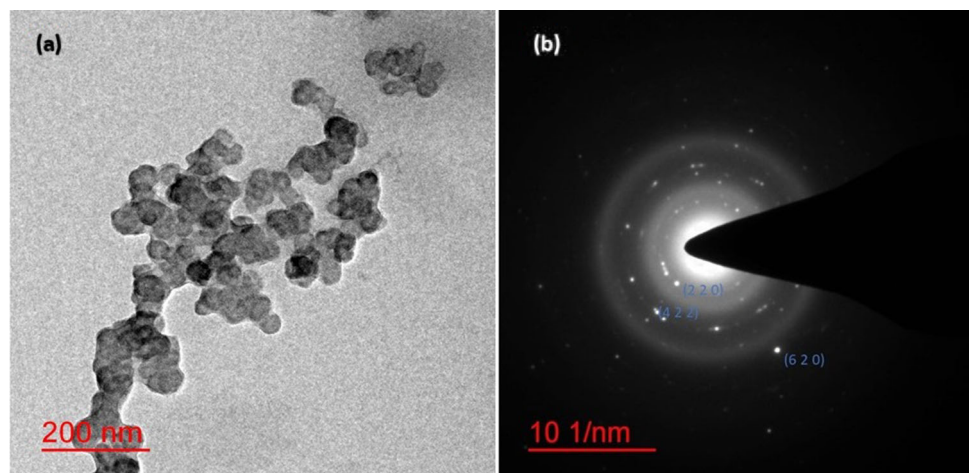
Figure 2 depicts the bright field image of BYCTO ceramics sintered at 1173 K for 8 h along with the corresponding selected electron area diffraction pattern. The nature of particles was found to be polycrystalline which is shown in Fig. 2a. The observed particle size was determined by TEM measurement with the help of Image J software and obtained to be in the range of 55 ± 7 nm. The calculated particle size from TEM was near the average crystallite size obtained from XRD. The selected electron area diffraction also confirmed the polycrystalline nature

of BYCTO ceramic shows bright spot patterns indicate corresponding planes (2 2 0) (4 2 2) and (6 2 0) which is mentioned in Fig. 2b.

4.2.2 High resolution scanning electron microscopic (SEM) studies

Figure 3a demonstrates the microstructure of the cleft surface of BYCTO which is sintered at 1173 K for 8 h. In the figure of the SEM image, we have seen some porosity that usually because of the exclusion of few substantial gases through the ignition of nitrate citrate precursor gel. It also clears from the figure grains exist in granular form with the polygonal shape which is well parted by grain boundaries. The average grains size of synthesized BYCTO ceramic was found to be $0.783 \mu m$ with the help of Image J software. The obtained grain size by SEM analysis is larger than that of crystallite size measured from XRD. The higher value of grain size is generally occurred due to the formation of a combination of some particles because, in the SEM instrument, the beam is scanned over the sample while in a TEM instrument, the beam passes through the sample. For this reason, the SEM image shows surface morphology and surface characteristics of the samples in form

Fig. 2 a Bright-field TEM image; b SAED pattern $Bi_{0.617}Y_{0.05}Cu_3Ti_4O_{12}$ ceramic sintered at 1173 K for 8 h



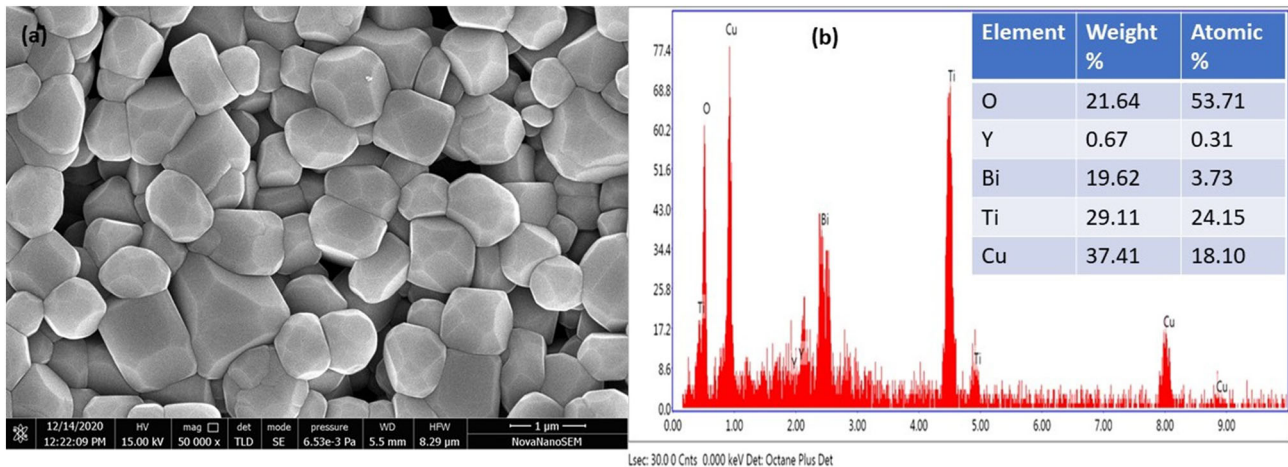


Fig. 3 The SEM micrograph and **b** EDX spectra corresponding $\text{Bi}_{0.617}\text{Y}_{0.05}\text{Cu}_3\text{Ti}_4\text{O}_{12}$ ceramics

of powder or film, while a TEM image displays internal structure and real particle sizes because of operating at high working potential. The origin of the differences in the particles sizes obtained by the SEM and TEM images can be understood from the step of sample supplying for these analyses, Therefore, the images obtained from TEM analysis have higher resolution and the agglomerations could be distinguished with this instrument, while in the SEM image, the agglomerated particles are usually observed with larger sizes (grain size). The chemical compositions and purity of the synthesized pallet were examined by EDX analysis. Figure 3b confirms the presence of Bi, Y, Cu, Ti, and O elements in the EDX spectrum of sintered BYCTO ceramic, and their atomic percentage, as well as weight percentage, were found to be 3.73, 0.31, 18.10, 24.15, 53.12 and 19.62, 0.67, 37.41, 29.11, 21.64, respectively [22].

4.2.3 Atomic force microscopic (AFM) studies

Figure 4a reveals a two-dimensional AFM image of BYCTO-sintered ceramic that exhibits the surface morphology of grains separated by grain boundaries. The AFM image shows plate-like grains parted by clear grain boundaries, the buffer layer, and a compact structure with granular morphology [30]. The maximum peak height of grains in the 3D image of AFM for BYCTO ceramics was determined to be $0.509 \mu\text{m}$ under scan area $10 \times 10 \text{ mm}^2$. The average and root mean square roughness was calculated to be $0.179 \mu\text{m}$ and $0.224 \mu\text{m}$ in the 3D surface roughness of BYCTO ceramic that is exhibited in Fig. 4b. The AFM investigation showed the existence of particles

in widespread size distribution in BYCTO ceramic. The average grain size was determined to be in the range of $0.5\text{--}1.0 \mu\text{m}$ out of 245 grains by the two-dimensional image of AFM as shown in histogram Fig. 4c which was also verified by SEM analysis. Figure 4d demonstrates the peak distribution curve of the 3D AFM image, highlighting the surface roughness of the BYCTO ceramic.

4.3 X-ray photoelectron spectroscopic (XPS) studies

The XPS spectrum of $\text{Bi}_{0.617}\text{Y}_{0.05}\text{Cu}_3\text{Ti}_4\text{O}_{12}$ (BYCTO) ceramic sintered at 1173 K for 8 h is visualized in Figs. 5a–e. In this study, we used Carbon 1 s as a reference, with the B.E. value of 284.58 eV to compensate for the charge effects of the surface. The presence of Bismuth Yttrium Copper Titanium and Oxygen required in the BYCTO ceramic have been confirmed by XPS analysis that reveals bismuth exist in + 3 oxidation state with binding energy 158.79 and 164.01 eV found at $\text{Bi } 4f_{5/2}$ and $\text{Bi } 4f_{7/2}$, respectively [28, 31]. This is shown in Fig. 5a. The XPS spectrum of Yttrium in BYCTO ceramic with binding energy is illustrated in Fig. 5b that established the presence of + 3 oxidation state of Yttrium having binding energy 158.78 eV corresponds to $\text{Y } 3d_{3/2}$ [32]. Figure 5c depicts the binding energies 933.77 eV and 953.70 eV corresponding to the $\text{Cu } 2p_{1/2}$ and $\text{Cu } 2p_{3/2}$ respectively with satellite peaks in the XPS spectrum of copper which exhibits that copper exists + 2 oxidation state in BYCTO ceramic [33]. The presence of satellites shake-up peaks at 940.5 eV, 941.1 eV and 943.5 eV, are related with Cu^{2+} oxidation state

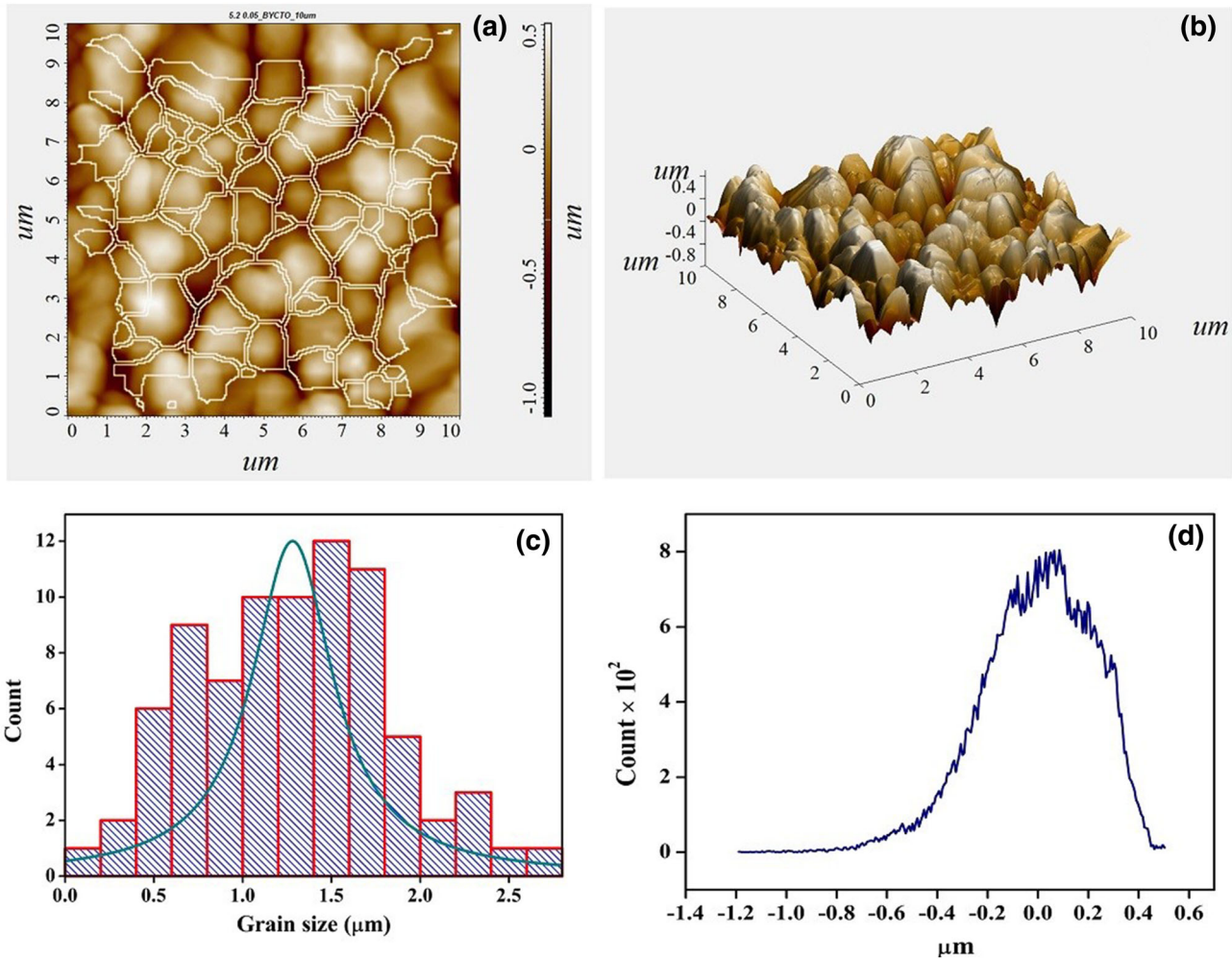


Fig. 4 AFM images of $\text{Bi}_{0.617}\text{Y}_{0.05}\text{Cu}_3\text{Ti}_4\text{O}_{12}$ ceramic, **a** two-dimensional image for grain boundary, **b** three-dimensional image for surface roughness, **c** depth histogram graph, and **d** bar diagram for particle size distribution

since these peak is characteristic of a partially filled d-orbital (d^9) and is not present in the d^{10} Cu + spectra [34]. Figure 5d displays the XPS spectrum of titanium of BYCTO which contributes four peak corresponding binding energies of 457.99 eV, 463.66 eV, 460.50 eV, and 466.42 eV, respectively. The first two binding energy peaks corresponding to the $\text{Ti } 2p_{3/2}$ and $\text{Ti } 2p_{1/2}$ confirmed the existence of + 4 oxidation state of Ti ion in the ceramic and the later two binding energy peak are related to the three valence state of Ti that denotes the existence of Ti^{+3} also in the ceramic [32, 34]. Figure 5e represents the O 1s core-level XPS peaks of BYCTO ceramic sintered for 8 h. It is clear from the figure that the two O 1s signals were observed which shows three different surface oxygen having different binding energies. The lower binding energy at 529.48 eV occurred due

to the lattice oxygen at the normal lattice site in the crystal structure that gives the information about hybridization of O 2p with transition metal ions. The binding energy peak at 530.87 eV is designated to the hydroxyl groups (OH) or cation-oxygen bond. However, the asymmetric behavior of high energy 532.77 eV in the O 1s XPS spectrum is consistent with the existence of the effect of absorbing H₂O or oxygen vacancy [35, 36].

4.4 Dielectric studies

Figure 6 illustrates temperature-dependent dielectric constant (ϵ' and dielectric loss ($\tan \delta$) of sintered BYCTO ceramic at few selected frequencies. It was observed that the dielectric permittivity nearly independent from 310 to 390 K at some selected frequencies. From Fig. 6a, we also found that the two

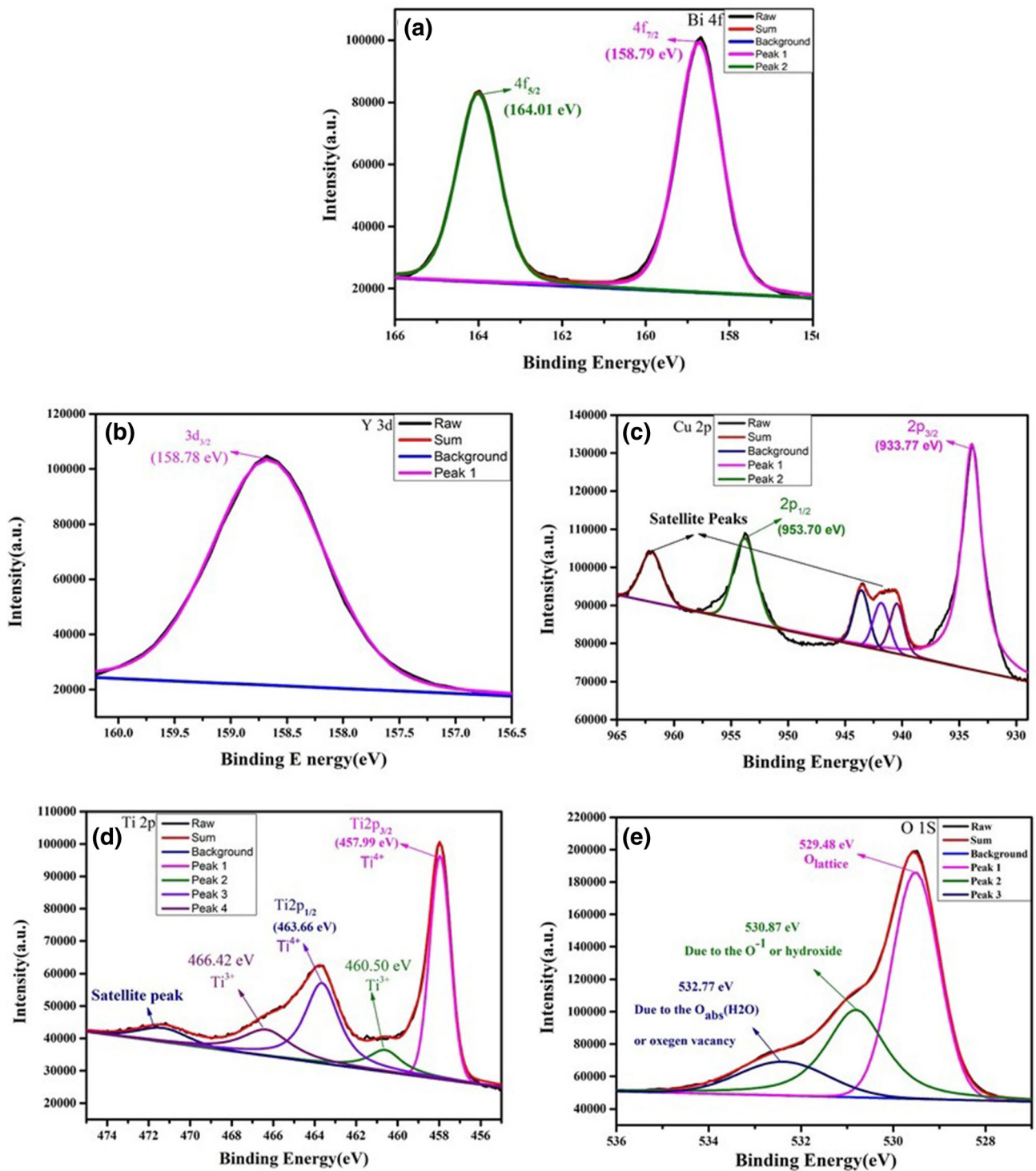


Fig. 5 XPS spectra of **a** Bi; **b** Y **c** Cu; **d** Ti; **e** O of $\text{Bi}_{0.617}\text{Y}_{0.05}\text{Cu}_3\text{Ti}_4\text{O}_{12}$ sintered ceramic

dielectric peaks at 415 and 450 K for all evaluated frequencies in which the first peak occurs corresponds to the ferroelectric-ferroelectric (FE-FE) and the second peak corresponding to the ferroelectric-paraelectric (FE-PE) phase transition [37]. It was as

well detected that the dielectric permittivity reduces employing rising frequency. The dielectric constant for sintered BYCTO ceramic was calculated to be 135.45, 127.46, and 112.67 at 1, 10, and 0.100 kHz, respectively. Figure 6b reveals the tangent loss ($\tan \delta$)

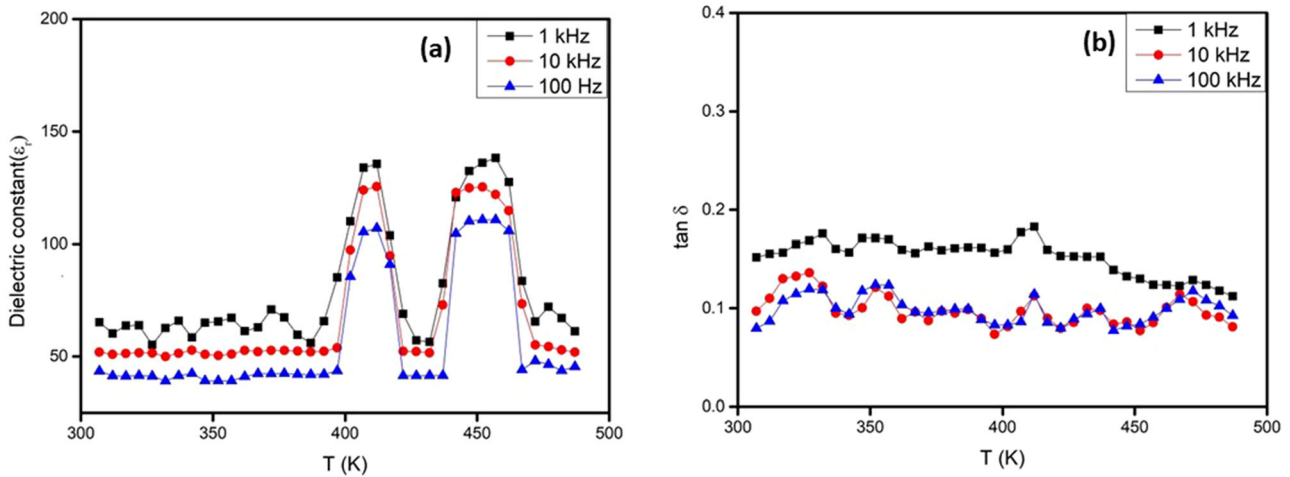


Fig. 6 Plot of **a** dielectric constant (ϵ'); **b** tangent loss ($\tan\delta$) vs temperature of $\text{Bi}_{0.617}\text{Y}_{0.05}\text{Cu}_3\text{Ti}_4\text{O}_{12}$ sintered ceramic at some measured frequency

of BYCTO ceramic at few selected temperatures for all measured frequencies [38]. It was observed that $\tan \delta$ increases from 310 K in the beginning and decreases after 360 K. The $\tan \delta$ loss was determined to be 0.07, 0.09 and 0.14 at 100 kHz, 10 kHz, and 1 kHz, respectively. Figure 7 represents the plot of dielectric constant and dielectric loss as a function of frequency for sintered BYCTO ceramics at some selected temperatures. The value of ϵ' was determined to be 1481, 741, 322, and 465 at 307 K, 367 K, 427 K, and 487 K, respectively. It is also clear from Fig. 7a that the ϵ' value sharply falls along with enhancing frequency till 10 kHz and afterward, it does not change much more, i.e., nearly constant on

the increasing frequency at all selected temperatures. Figure 7b shows that the dielectric loss rapidly decreases up to 10 kHz and after that, it continues constantly in a higher frequency range at all measured temperatures. The values of tangent loss of BYCTO were found to be in the range of 0.13 to 0.29 at 10 kHz from 307 to 487 K. The space charge polarization is responsible for the decrement of dielectric constant with frequency. Since in lower frequency range, the charges generate more electronic polarization because it has more time to cover a longer distance in the materials and consequently dielectric constant increases. In the higher frequency region, the dielectric permittivity does not change

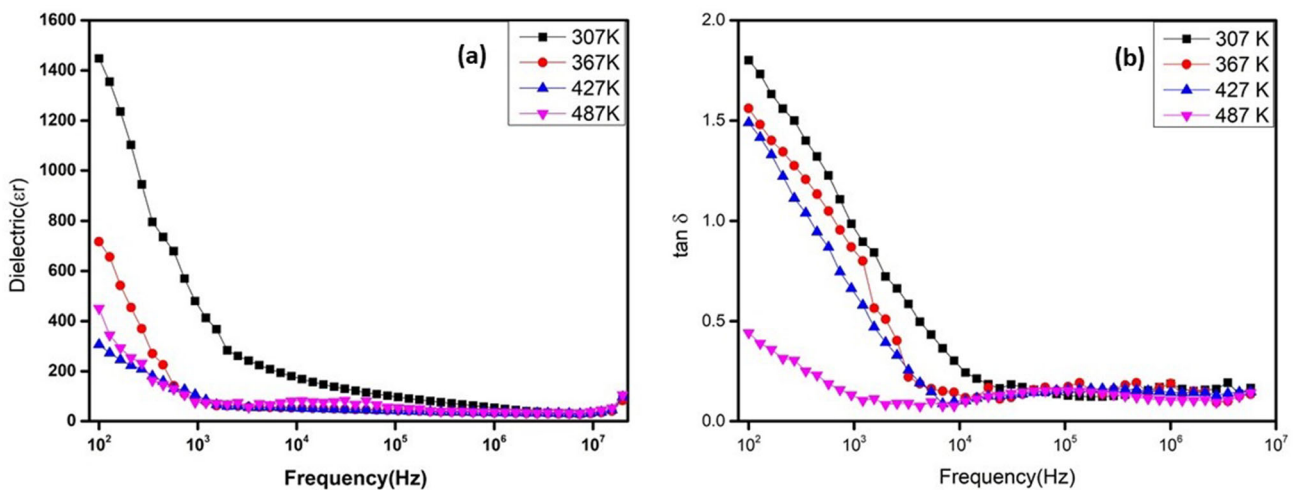


Fig. 7 Frequency dependence of **a** dielectric constant (ϵ'); **b** dielectric loss ($\tan\delta$) of $\text{Bi}_{0.617}\text{Y}_{0.05}\text{Cu}_3\text{Ti}_4\text{O}_{12}$ ceramics at a few selected temperatures

much more because of space charge no longer follows the external electric field means no charge accumulates at the interface [22, 24].

4.5 Impedance spectroscopy studies

Complex impedance spectroscopy (CIS) is one of the most efficient methods to knowing the dielectric depression and the existence of the internal barrier layer generally occurs due to the contribution of grains and grain boundaries in perovskites ceramic materials and Information regarding the simultaneous occurrence of multi-polarization processes and their relaxation conditions can be obtained [39]. It can also be determined the effective involvement of grains, grain boundaries, and electrode interface specimen to the total resistance as well as capacitance, respectively. All the three contributions in the complex impedance plot are done by the semi-circular arc and occur at different frequency regions, i.e., at lower frequency region, grains contribution occurs and at middle frequency region, grain boundaries contribution occurs but at higher frequency region, the electrode contribution takes place, respectively. Figure 8a shows the CIS plot of BYCTO-sintered ceramic for 8 h at some selected temperatures (307–487 K). It indicated the existence of one semi-circular arc having different intercepts because of grain boundaries. The graph reveals the inset data of complex impedance plot through expanded view in higher frequency region which providing non-zero intercepts on z-axis by extrapolation that suggest

another semi-circular arc in the higher frequency region. These non-zero intercepts provided grain resistance. The values of grains and grain boundaries resistance can be calculated from the following equation,

$$Z^* = \frac{1}{R_g^{-1} + i\omega C_g} + \frac{1}{R_{gb}^{-1} + i\omega C_{gb}} = Z' - iZ'' \tag{5}$$

where

$$Z' = \frac{R_g}{1 + (\omega R_g C_g)^2} + \frac{R_{gb}}{1 + (\omega R_{gb} C_{gb})^2} \tag{6}$$

and

$$Z'' = R_g \left[\frac{\omega R_g C_g}{1 + (\omega R_g C_g)^2} \right] + R_{gb} \left[\frac{\omega R_{gb} C_{gb}}{1 + (\omega R_{gb} C_{gb})^2} \right] \tag{7}$$

where R_g , R_{gb} , C_g , and C_{gb} are the grain resistance, grain boundary resistance, the capacitance of grain, and grain boundary. The $\omega = 2\pi f$ represents the angular frequency. From the inset figure values of grains, resistance were found to be 457.62 Ω , 384.89 Ω , 349.34 Ω and 250.16 Ω at 307 K, 367 K, 427 K, and 487 K, respectively. On the increasing temperature, it was found that the size of the arc decreases, i.e., resistance decreases that means the grain boundaries resistance reduces [40]. At different temperatures, the values of grain boundaries resistance can be calculated from arcs which are shown in Fig. 8a and we were found to be 1,569,905.96 Ω , 1,642,633.23 Ω , 1,722,466.04 Ω and 1,880,041.8 Ω at 487 K, 427 K, 367 K and 307 K, respectively. It was also observed that the high value of grain boundaries resistance

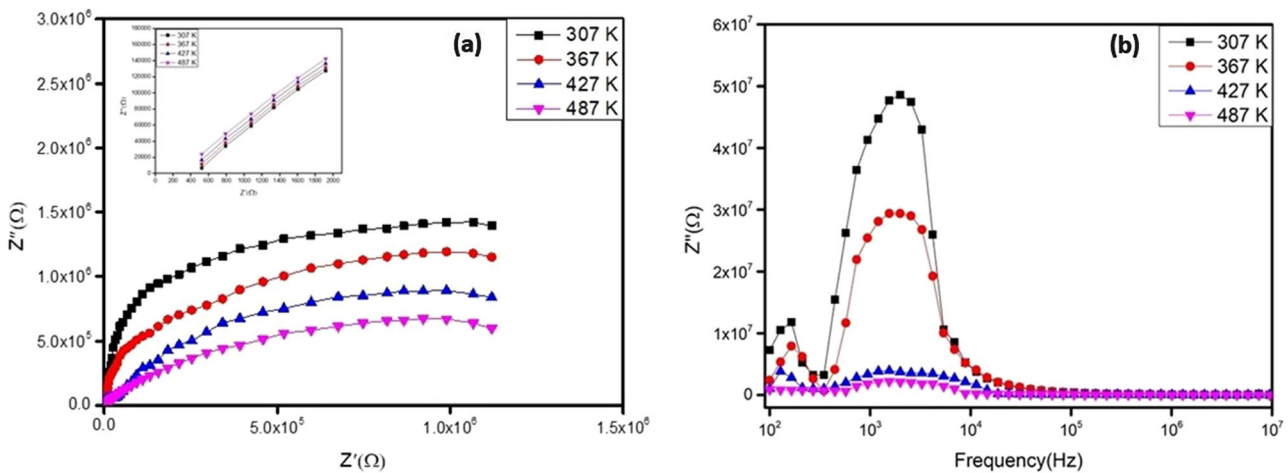


Fig. 8 **a** complex Impedance plane plots (Z' vs Z'') at few selected temperatures **b** Plots of imaginary impedance (Z'') with frequency at few measured temperatures of $\text{Bi}_{0.617}\text{Y}_{0.05}\text{Cu}_3\text{Ti}_4\text{O}_{12}$ ceramic

decreased the arc of the grains in the higher frequency region. This is related to the Internal Barrier layer Capacitance (IBLC) phenomenon and that tells the information about conducting behaviour of grains parted by insulating grain boundaries [41].

Figure 8b represents the variation of impedance (Z'') with frequency at some selected. In this figure, we were observed that the values of Z'' decreased with raising frequency and in higher frequency regions, it was been collapse to each other. From the figure, it was observed the appearance of two relaxation peaks at all measured temperatures one at 191 Hz and the other at 2.226 kHz. The first relaxation peak in the lower frequency region was obtained due to the electrode phenomenon and another peak was observed around 2.226 kHz because of the grain boundaries effect [22]. On the increasing temperature, the suppression of relaxation peaks was observed in a higher frequency region that explains the existence of temperature-dependent Maxwell–Wagner dielectric relaxation. [22]

4.6 Conductivity measurement

Figure 9a reveals the trend of temperature-dependent conductivity (DC) of sintered BYCTO ceramic at different frequencies, i.e., $\ln \sigma$ vs $1000/T$. In this figure, we were observed that the conductivity surge with increasing temperature. This conductivity can be fitted by the Arrhenius equation as,

$$\sigma = \sigma_0 \exp(-E_a/k_B T) \quad (8)$$

where E_a , σ_0 , k_B , and T are the activation energy related to the conduction process, pre-exponential factor, Boltzmann constant, and absolute temperature. From the figure, it was observed that activation energy slow down on raising frequency. The activation energy for ionic conduction was found to be 0.212 eV, 0.209 eV, and 0.152 eV at 1 kHz, 10 kHz, and 100 kHz, respectively. This occurs because of the improvement of electronic jumps on increasing the applied frequency [41]. The $\ln \sigma_{AC}$ vs $\ln \omega$ plot of BYCTO-sintered ceramic samples at different temperatures is illustrated in Fig. 9b. It was found that at all frequencies, the conductance spectra do not converge. This shows that the AC conductivity dependent on temperatures at all frequencies. The conductivity behaviours in a sample related to AC contribution followed the universal power law,

$$\sigma_{AC}(\omega) = \sigma_0 + A\omega^s \quad (9)$$

where σ_0 and A are the DC conductivity and pre-exponential factors. The factor s gives information about the degree of interaction between the mobile ions, also called a pre-exponential factor and its value is lower than 1 [38]. From Fig. 9b, we have calculated the value of s with the help of Eq. 2 by plotting the slope $\ln \sigma_{AC}$ vs $\ln \omega$ for BYCTO-sintered ceramic. The values of s were extracted 0.839, 0.806, 0.751 and 0.719 at 307 K, 367 K, 427 K, and 487 K, respectively. This indicates that the frequency dependence of σ_{AC} can be explained in terms of the correlated barrier hopping (CBH) model [42].

4.7 Optical properties

Diffuse reflectance ultraviolet–visible spectrophotometry (DRS) is used to determine the optical properties of the samples. Figure 10 shows the DRS UV–Vis spectra of $\text{Bi}_{0.617}\text{Y}_{0.05}\text{Cu}_3\text{Ti}_4\text{O}_{12}$ (BYCTO) nanoparticles. The optical bandgap value of the BYCTO ceramic is varying that depend upon the size of the nanoparticle prepared and the corresponding synthesis process. In the present experiment, we have adopted Kubelka–Munk theory for the determination of optical bandgap value of BYCTO nanoparticles, from recorded diffuse reflectance spectra. The exponent n in Eq. 3 described in the introduction section, can be determined from the plot of $(F(R).hv)^n$ vs. hv . The best fit to the straight line near the onset of absorption, observed for $n = 1/2$ recommending indirect allowed transition for BYCTO nanoparticle.

From the plot of $(F(R).hv)^{1/2}$ vs. hv (inset figure) the bandgap value of the prepared BYCTO nanoparticle is calculated to be 5.02 eV, from the extrapolation of the linear region of the curve.

5 Conclusion

In this study, BYCTO was synthesized by an economically semi-wet route using metal nitrate solution and TiO_2 powder. The single-phase formation of BYCTO was established by XRD and the average crystallite size was calculated to be 53 nm with the help of the XRD result, which is in good agreement with particle size (55 nm–94 nm) found by TEM measurement. The average grain size of BYCTO

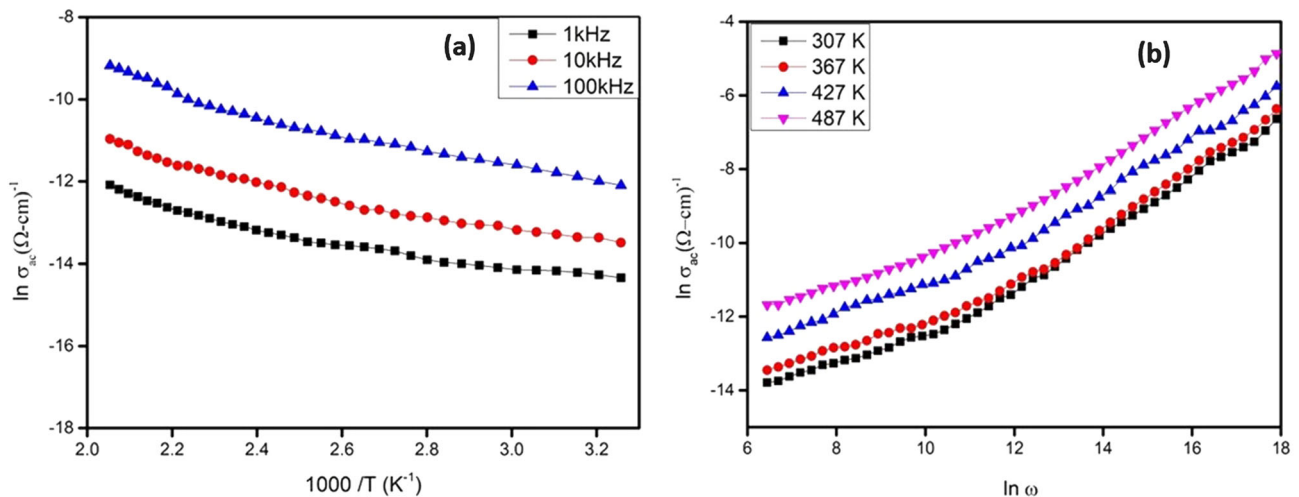


Fig. 9 **a** Plots of conductivity ($\ln \sigma$) with the inverse of temperature at few selected frequencies; **b** frequency dependence of AC conductivity at some designated temperatures of $\text{Bi}_{0.617}\text{Y}_{0.05}\text{Cu}_3\text{Ti}_4\text{O}_{12}$ ceramics

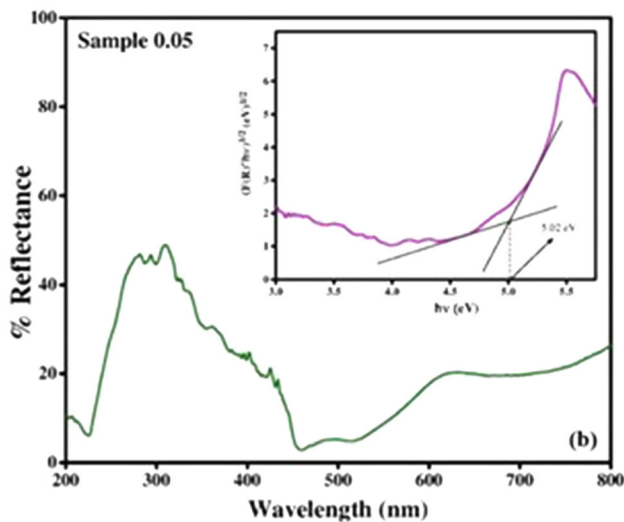


Fig. 10 Diffuse reflectance spectra of $\text{Bi}_{0.617}\text{Y}_{0.05}\text{Cu}_3\text{Ti}_4\text{O}_{12}$ sintered ceramic

ceramic sintered at 1273 K for 8 h was calculated to be 0.783 μm and fine grain boundaries and correspondingly supported by AFM analysis. The dielectric constant and tangent loss were found to be temperature independent in the higher frequency range and temperature dependent in the lower frequency range. The conformation of Bi, Y, Cu, Ti, and O elements and their atomic percentage present in ceramic materials were determined with the help of the EDX spectrum. The impedance of BYCTO ceramic reveals the contribution associated with the grain boundaries. Correlated Barrier Hopping (CBH)

models were used to explain the AC conductivity and frequency exponent parameters.

Acknowledgements

The author is grateful to the Central Instrument Facility Centre (CIFC) IIT (BHU) Varanasi for providing SEM, TEM, AFM, EDX, and XPS facilities.

Declarations

Conflict of interest The authors state that there is no brawl among them concerning the publication of this article.

References

1. K. Sun, L.F. Xu, C. Mao, X. Feng, J.Y. Liang, H.B. Xiao, R.L. Wang, D.W. Shi, C.P. Yang, *J. Alloys Compd.* **704**, 676 (2017)
2. P. Mao, J. Wang, S. Liu, L. Zhang, Y. Zhao, L. He, *J. Alloys Compd.* **778**, 625 (2019)
3. L.C. Kretly, A.F.L. Almeida, P.B.A. Fachine, R.S. De Oliveira, A.S.B. Sombra, *J. Mater. Sci.* **15**, 657 (2004)
4. R. K. Pandey, W. A. Stapleton, J. Tate, A. K. Bandyopadhyay, I. Sutanto, S. Sprissler, and S. Lin, *AIP Adv.* **3**, 0 (2013).
5. S. Rani, N. Ahlawat, K.M. Sangwan, S. Rani, R. Punia, J. Malik, *J. Mater. Sci. Mater.* **29**, 10825 (2018)
6. L. Singh, B.C. Sin, I.W. Kim, K.D. Mandal, H. Chung, Y. Lee, *J. Am. Ceram. Soc.* **99**, 27 (2016)

7. M.A. Subramanian, D. Li, N. Duan, B.A. Reisner, A.W. Sleight, *J. Solid State Chem.* **151**, 323 (2000)
8. C. Kai, L. Wei, L. Yun-Fei, B. Peng, L. Xiao-Mei, Z. Jin-Song, *Chin. Phys. Lett.* **21**, 1815 (2004)
9. M. Li, A. Feteira, D.C. Sinclair, A.R. West, *Appl. Phys. Lett.* **88**, 1 (2006)
10. M. H. Cohen, J. B. Neaton, L. He, D. Vanderbilt, M. H. Cohen, J. B. Neaton, L. He, and D. Vanderbilt, **3299**, (2012).
11. M. Li, Z. Shen, M. Nygren, A. Feteira, D. C. Sinclair, and A. R. West, *J. Appl. Phys.* **106**, (2009).
12. P.R. Bueno, R. Tararan, R. Parra, E. Joanni, M.A. Ramírez, W.C. Ribeiro, E. Longo, J.A. Varela, *J. Phys. D* **42**, 055404 (2009)
13. D.C. Sinclair, T.B. Adams, F.D. Morrison, A.R. West, *Appl. Phys. Lett.* **80**, 2153 (2002)
14. W. Li, R.W. Schwartz, *Appl. Phys. Lett.* **89**, 87 (2006)
15. Y.Q. Tan, J.L. Zhang, W.T. Hao, G. Chen, W.B. Su, C.L. Wang, *Mater. Chem. Phys.* **124**, 1100 (2010)
16. Z. Yang, P. Liang, L. Yang, P. Shi, X. Chao, Z. Yang, *J. Mater. Sci. Mater.* **26**, 1959 (2015)
17. L. Yang, X. Chao, Z. Yang, N. Zhao, L. Wei, Z. Yang, *Ceram. Int.* **42**, 2526 (2016)
18. L. Yang, G. Huang, T. Wang, H. Hao, Y. Tian, *Ceram. Int.* **42**, 9935 (2016)
19. L. Sun, Z. Wang, W. Hao, E. Cao, Y. Zhang, H. Peng, *J. Alloys Compd.* **651**, 283 (2015)
20. V.S. Saji, H.C. Choe, *Thin Solid Films* **517**, 3896 (2009)
21. F. Luo, J. He, J. Hu, Y.H. Lin, *J. Am. Ceram. Soc.* **93**, 3043 (2010)
22. S. Sharma, S.S. Yadav, M.M. Singh, K.D. Mandal, *J. Adv. Dielectr.* **04**, 1450030 (2014)
23. J. Liu, C.G. Duan, W.G. Yin, W.N. Mei, R.W. Smith, J.R. Hardy, *Phys. Rev. B* **70**, 1 (2004)
24. P. Gautam, A. Khare, S. Sharma, N.B. Singh, K.D. Mandal, *Prog. Nat. Sci. Mater. Int.* **26**, 567 (2016)
25. M. M. Ahmad and K. Yamada, *J. Appl. Phys.* **115** (2014).
26. M.M. Ahmad, E. Al-Libidi, A. Al-Jaafari, S. Ghazanfar, K. Yamada, *Appl. Phys. A* **116**, 1299 (2014)
27. V. Kumar, S. Pandey, A. Kumar, M.K. Verma, S. Singh, V.S. Rai, D. Prajapati, T. Das, A. Sharma, C.L. Prajapat, A. Gangwar, K.D. Mandal, *J. Mater. Res. Technol.* **9**, 12936 (2020)
28. V. S. Rai, S. Pandey, V. Kumar, M. K. Verma, A. Kumar, S. Singh, D. Prajapati, and K. D. Mandal, *J. Mater. Sci. Mater. Electron.* **12**, (2020).
29. T. T. Carol T, J. Mohammed, R. Bhargava, S. Khan, S. Mishra, S. K. Godara, and A. K. Srivastava, *Mater. Chem. Phys.* **248**, 122933 (2020).
30. R.K. Nimat, R.S. Joshi, S.H. Pawar, *J. Alloys Compd.* **466**, 341 (2008)
31. Y. Zhao, B. Yang, Q. Wu, Y. Zhou, F. Guo, and S. Zhao, *Nanoscale* (2021).
32. L. Singh, M. Sheeraz, M.N. Chowdhury, U.S. Rai, S.S. Yadava, Y.S. Park, S.V. Singh, Y. Lee, *J. Mater. Sci. Mater.* **29**, 10082 (2018)
33. S. Pandey, V. Kumar, V.K. Sharma, K.D. Mandal, *Mater. Chem. Phys.* **253**, 123384 (2020)
34. M. Claros, M. Setka, Y.P. Jimenez, S. Vallejos, *Nanomaterials* **10**, 1 (2020)
35. V. Kumar, A. Kumar, M. K. Verma, S. Singh, S. Pandey, V. S. Rai, D. Prajapati, T. Das, N. B. Singh, and K. D. Mandal, *Mater. Chem. Phys.* **245** (2020).
36. S. Jaiswar, K.D. Mandal, *J. Phys. Chem. C* **121**, 19586 (2017)
37. S. Thakur, R. Rai, I. Bdikin, M.A. Valente, *Mater. Res.* **19**, 1 (2016)
38. S.B.R.S. Adnan, N.S. Mohamed, *Ceram. Int.* **40**, 11441 (2014)
39. M. Veith, S. Ren, M. Wittmar, H. Bolz, *J. Solid State Chem.* **182**, 2930 (2009)
40. M. M. Costa, G. F. M. Pires, A. J. Terezo, M. P. F. Graa, and A. S. B. Sombra, *J. Appl. Phys.* **110** (2011).
41. A. Kumar, S.S. Yadava, P. Gautam, A. Khare, K.D. Mandal, *J. Electroceram.* **42**, 47 (2019)
42. R. Jana, J. Datta, S. Sil, A. Dey, B. Pal, A. Biswas, and P. P. Ray, *Mater. Res. Express* **6** (2019).

Publisher's Note Springer Nature remains neutral with regard to jurisdictional claims in published maps and institutional affiliations.